PROCEEDINGS, 50th Workshop on Geothermal Reservoir Engineering
Stanford University, Stanford, California, February 10-12, 2025
SGP-TR-229

A Coupled Hydro-Mechanical Analysis of Impact of DFN on Reservoir Stimulation at FORGE

Hafssa Tounsi[1,*], Branko Damjanac[1], Zorica Radakovic-Guzina[1], Wei Fu[1], Aleta Finnila[2], Pengju Xing[3], Robert Podgorney[4]

[1] Itasca Consulting Group, Inc., Minneapolis, MN, USA

[2] WSP USA Inc., Redmond, WA, USA

[3] Energy & Geoscience Institute, University of Utah, Salt Lake City, UT, USA

[4] Idaho National Laboratory, Idaho Falls, ID, USA

[*] htounsi@oneitasca.com

Keywords: Discrete Fracture Network (DFN), Enhanced Geothermal System (EGS), Hydraulic Fracturing (HF), Numerical Modeling, Hydro-Mechanical Coupling.

ABSTRACT

The Utah Frontier Observatory for Research in Geothermal Energy (FORGE) project conducted an eight-stage, commercial-scale hydraulic stimulation of the geothermal reservoir from the injection well 16A(78)-32 in 2024, aiming to establish connectivity with production well 16B(78)-32 and increase the permeability of the geothermal reservoir between the wells. Fiber optic monitoring during the stimulation and subsequent circulation tests confirmed multiple fractures (created or reactivated) intersecting the production well.

This paper analyzes the reservoir stimulation, considering hydraulic fracturing and reactivation of pre-existing natural fractures (discrete fracture network, DFN). The analysis uses XSite, a numerical software, to simulate hydraulic fracturing in naturally fractured rock masses. XSite employs the lattice approach to implement the synthetic rock mass (SRM) method. Fully coupled hydro-mechanical simulations were conducted for three single-cluster stages (stages 4, 5 and 10) and two multi-cluster stages (stages 8 and 9), with predicted bottomhole pressures compared to field data.

The data on hydraulic and natural fracture geometries and interactions are limited. The DFN geometrical properties, characterized by using borehole logs, are inherently variable and stochastic. The DFN hydromechanical properties are also uncertain and variable, and difficult to characterize on the relevant scale. To better understand the injection pressure measurements, three DFN scenarios and one sensitivity case were explored: 1) permeable and frictional DFN, 2) permeable and cohesive DFN, 3) impermeable and cohesive DFN, and 4) a variant of the impermeable and cohesive DFN with reduced initial aperture (compared to scenario 3). Our findings indicate that DFN characteristics significantly influence reservoir stimulation and injection pressure history. The impermeable and cohesive DFN scenario with reduced aperture best matches the observed long-term bottomhole pressures in most stages. Additionally, fluid migration patterns deviated from classical hydraulic fracture growth, as confirmed by fiber optic monitoring, which detected fracture intersections with the production well misaligned with the injection clusters on the injection well. This further emphasizes the role of natural fractures in response of the reservoir to fluid injection and in creating connectivity. These results highlight the need for continued refinement of DFN modeling to improve predictive capabilities in naturally fractured reservoirs and similar rock types.

1. INTRODUCTION

The April 2024 hydraulic stimulation campaign at the Utah FORGE site aimed to enhance connectivity and permeability between injection well 16A(78)-32 and production well 16B(78)-32. As shown in Figure 1, well 16A(78)-32 is deviated at a 65° angle from vertical after reaching a depth of 1,829 m (6,000 ft), with its deviated section located approximately 100 m (330 ft) below the corresponding section of well 16B(78)-32. Hydraulic connectivity between the two wells was improved by inducing fractures and stimulating pre-existing natural fractures in the rock mass.

The campaign involved seven stimulation stages in the cased section of well 16A(78)-32. The dotted section of well 16A(78)-32 in Figure 1 highlights the stimulated area. This analysis focuses on stages 4, 5, 8, 9, and 10. Stages 6 and 7 were shut down prematurely due to insufficient pumping rates for fracture propagation. Table 1 summarizes the cluster spacing, depths, pumping fluids, and pumping rates for the analyzed stages. Stages 4 and 5, as well as stages 8 and 9, were conducted under similar conditions, differing primarily in the type of pumping fluid used.

To track fracture propagation and interwell connectivity, treating pressure measurements, Distributed Acoustic Sensing (DAS), and microseismic monitoring (Niemz et al., 2025) were employed. A fiber optic DAS cable, cemented behind the casing of well 16B(78)-32, recorded strain variations during the stimulation from injection well 16A(78)-32. Large strain changes were identified as potential fracture intersections with the production well. Figure 2 illustrates the stimulation stages of well 16A(78)-32 and the corresponding intersection locations in well 16B(78)-32. These identified intersections guided the selection of perforation and injection intervals for the stimulation from well 16B(78)-32. The combined monitoring data, including DAS and microseismic monitoring, confirmed the interwell connectivity.

Figure 2 also shows that fracture hit locations recorded in the production well during Stages 8 and 9 do not align with the corresponding injection clusters. This suggests that fluid migration did not follow classical pattern of planar vertical hydraulic fractures but was instead influenced by the discrete fracture network (DFN), which played a major role in shaping the complex fluid flow paths.

This paper investigates the influence of the natural fracture network on hydraulic connectivity by comparing the fiber optic data and injection pressure histories with results of the coupled hydro-mechanical numerical modeling. The study aims to improve understanding of EGS response to fluid injection as a function of DFN hydromechanical properties. The variations in injection pressure histories and reservoir stimulation (fracture propagation and reactivation) were analyzed across different DFN configurations, ranging from impermeable cohesive to permeable frictional DFNs.

Following an introduction to XSite, the numerical modeling software used, the paper presents the model setup, simulation results, and a comparison with field data.

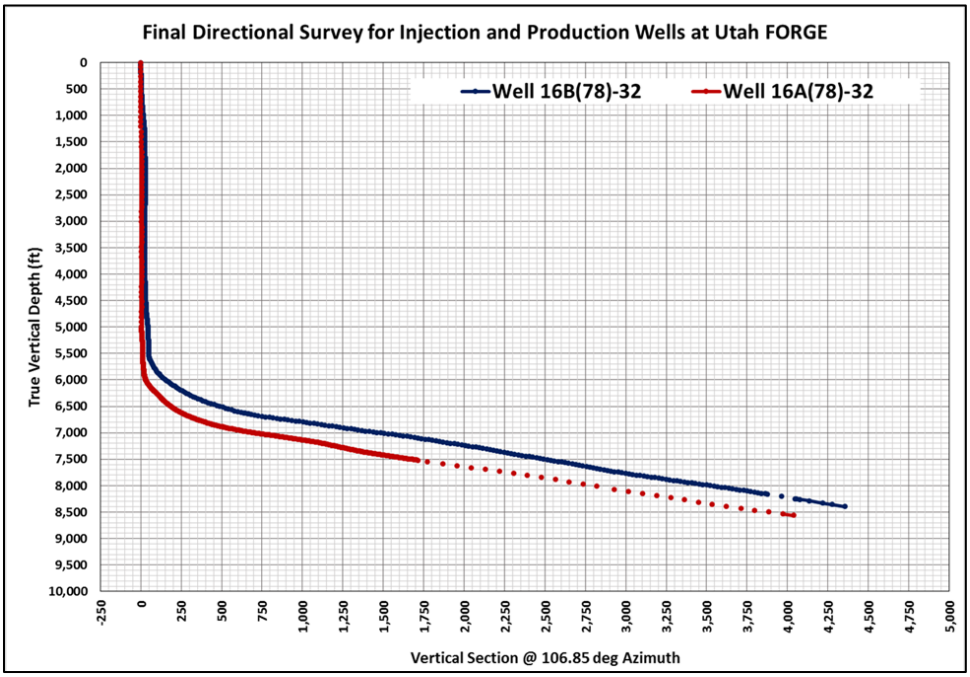

Figure 1 : Trajectory of wells 16A(78)-32 and 16B(78)-32 (McLennan et al., 2024).

Table 1: Field pumping information for the five analyzed stimulation stages.

Stage name	Number of clusters	Clusters spacing (m)	Pumping fluid	Maximum pumping rate (bpm)	Measured Depth (m)
Stage 4	1	-	Slickwater	35	3,070 (10,072 ft)
Stage 5	1	-	XL CMHPG	35	3,055 (10,022 ft)
Stage 8	8	7.6 (25 ft)	XL CMHPG	80	2,910 – 2,963 (9,547 - 9,722 ft)
Stage 9	8	7.6 (25 ft)	Slickwater	80	2,841 – 2,895 (9,322 - 9,497 ft)
Stage 10	1	-	Slickwater	35	2,826 (9,272 ft)

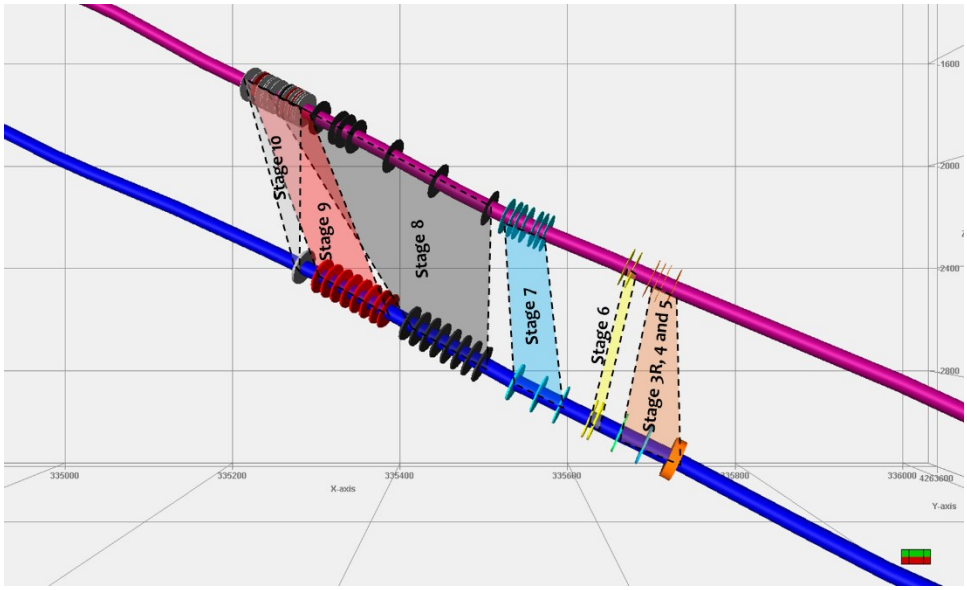

Figure 2 : Approximate intervals of cross-well fracture intersections identified from fiber optic data during Stages 4 to 10. (created by Schlumberger's Petrel software)

2. SIMULATION OF THE APRIL 2024 STIMULATION TEST AT FORGE

2.1 Numerical Model

Coupled hydro-mechanical simulations of fluid injection and hydraulic fracture propagation in a fractured reservoir were conducted using XSite, a Discrete Element Method (DEM) code developed by Itasca Consulting Group (Itasca, 2023). XSite employs the Synthetic Rock Mass (SRM) method and a lattice numerical approach to model deformation, hydraulic fracture propagation, and related microseismicity in naturally fractured reservoirs. Its capabilities have been verified for viscosity-dominated and toughness-dominated hydraulic fracturing regimes and the interaction of hydraulic fractures with existing fractures (Damjanac and Cundall, 2016; Fu et al., 2016, 2019). The thermal effects were not considered in this study because they were not considered significant for the injection durations.

2.1 Model Setup

The model simulates a fractured granitic rock volume with dimensions of 600 m × 600 m × 600 m, with the top located at an approximate depth of 2,200 m (7,218 ft). The domain is rotated by 25° from the N-S direction to align with the principal stress directions. This setup encompasses the stimulated volume between the injection well and the production well. The well trajectories for 16A(78)-32 and 16B(78)-32 were incorporated into the model geometry, though near-wellbore fracture initiation and perforation effects, as described by Fu et al. (2024), were not explicitly modeled. Perforation clusters were represented as spherical zones, with fracturing initiated from circular startup joints of 4 m radius. Six perforations were assumed to actively take fluid for each cluster. Pressure drop across the perforation tunnels in well 16A(78)-32 was considered in the multi-cluster stages only (Stages 8 and 9).

The DFN consists of 17,855 natural fractures. Most of the fractures were stochastically generated and iteratively updated using microseismic data from the April 2022 stimulation (Finnila et al., 2021; Finnila and Jones, 2024). These updates involved fitting fracture planes to the microseismic catalog and adding tensile fractures observed during stimulation. Fracture sizes range from 10 m to 150 m in equivalent radius. Initial fracture apertures were calibrated by Finnila and Jones (2024), based on bulk rock porosity (1-2%) and assumed fracture aperture-size relationships, with apertures ranging from 0.1 mm to 0.65 mm.

Stages 4 and 5 (one model) and Stage 8, 9, and 10 (another model) were modeled in sequence in two separate models to account for stress shadow effects during stimulation. Two subdomains were created around these stages (see Figure 3), with dimensions of approximately 140 m (width), 230 m (height), and 200 m (length for Stages 8-10; half the length for Stages 4-5). The tops of the subdomains are located at depths of 2,480 m and 2,400 m for Stages 4-5 and 8-10, respectively. Inside each subdomain, a 2 m lattice resolution was used, gradually increasing to 12 m in the main domain. This setup ensured the computational efficiency of simulations, by preventing unrealistic cracking around natural fractures far from the stimulation area, while capturing the extent of stimulation.

Rock and fluid properties and in-situ stress magnitudes are summarized in Table 2. The pre-existing fracture properties are detailed in Table 3. Three DFN scenarios were considered: 1) impermeable cohesive (Imp. Coh. DFN), 2) permeable cohesive (Perm. Coh. DFN), and 3) permeable frictional (Perm. Fric. DFN). The impermeable cohesive DFN scenario assumes fractures are impermeable initially, becoming permeable only after their failure. The permeable, cohesive and permeable, frictional DFNs are permeable under initial conditions.

The hydraulic fracture that appears to have been created from Stage 3 in April 2022 was included in the DFN. It was assumed to be permeable and frictional in all scenarios. This fracture, shown as the uncropped, orange-colored fracture in Figure 3, was assigned the same friction angle and stiffness values as the DFN.

To assess the impact of the initial fracture apertures, a sensitivity analysis was conducted for the impermeable cohesive DFN scenario by running an additional case, where the DFN fracture (including the hydraulic fracture from Stage 3) apertures were reduced by a factor of 10 (this scenario will be referred to by Imp. Coh. DFN; Ap./10 in the results section).

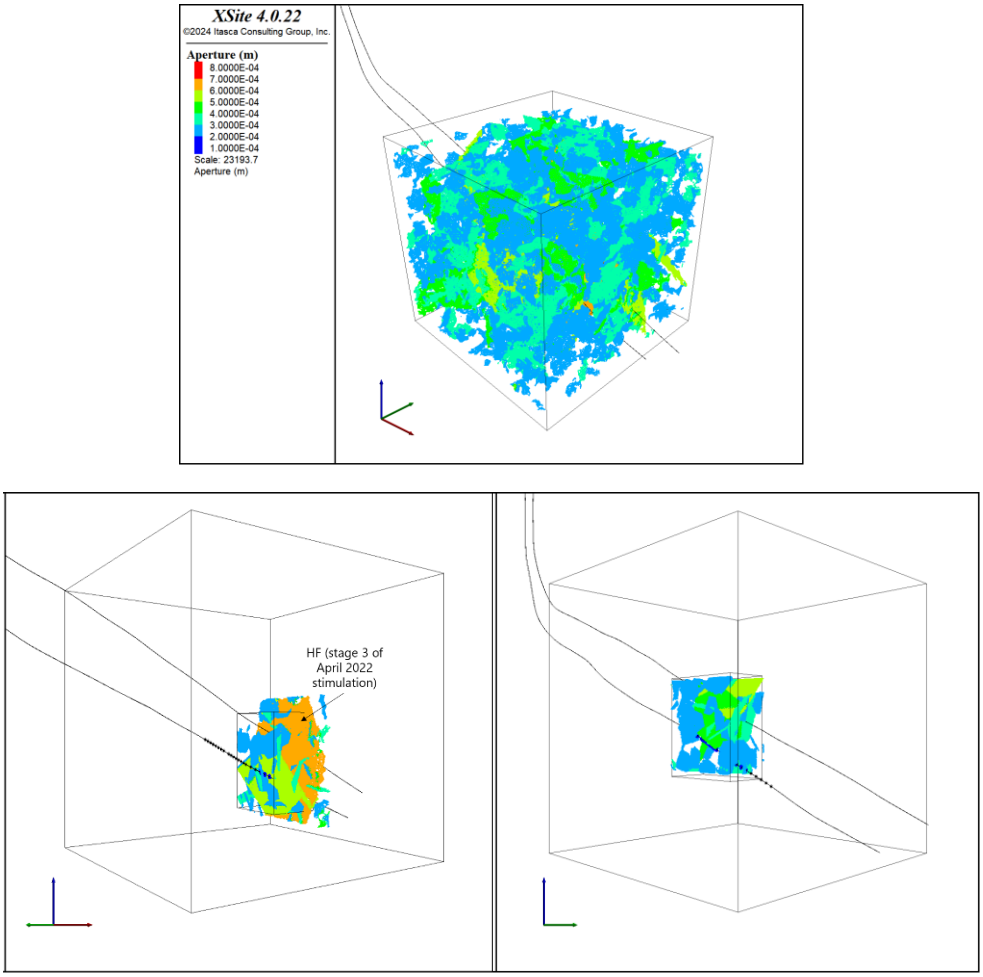

Figure 3: Numerical model domain. The top image shows the full DFN and the initial aperture distribution. The bottom images illustrate the subdomains used in the simulations: the left image corresponds to the Stages 4-5 simulation, and the right image to the Stages 8-9-10 simulation, with the cropped DFN inside the subdomains. The bottom left image also shows the uncropped hydraulic fracture (HF) inherited from the Stage 3 April 2022 stimulation.

Table 2: Rock properties and initial conditions.

Parameter	**Schistose Quartzite**	
Young's modulus, GPa	55	
Poisson's ratio	0.26	
Tensile Strength, MPa	10	
Fracture toughness, MPa.m$^{1/2}$	3	
Fluid viscosity, cP	Slickwater	2
	Linear Gel	25

Pore pressure, MPa/m	0.00981
Minimum horizontal stress gradient, MPa/m	0.017 – Dip Direction N115°E
Maximum horizontal stress gradient, MPa/m	0.02 - Dip Direction N25°E
Vertical stress gradient, MPa/m	0.026

Table 3: Fracture properties.

Parameter	**Impermeable Cohesive DFN (Imp. Coh. DFN)**	**Permeable Cohesive DFN (Perm. Coh. DFN)**	**Permeable Frictional DFN (Perm. Fric. DFN)**
Normal Stiffness, MPa/m	100		
Shear Stiffness, MPa/m	100		
Friction angle, °	37		
Cohesion, MPa	20		0
Tensile strength, MPa	10		0

2.2 Results and Discussion

To compare the wellhead treating pressure recorded during stimulation with the bottomhole pressure predicted by XSite, the wellhead pressure was adjusted to account for hydrostatic and frictional losses within the wellbore. Hydrostatic pressure is calculated based on the fluid density and the depth of the injection zone, while frictional losses are derived from the pumping step-down data at the end of the stimulation (Xing et al., 2023). These components are used to estimate the bottomhole pressure, compared with the model's predictions.

2.2.1 Stages 4 and 5

The pressure and pumping rate histories for Stages 4 and 5 are shown in Figures 4 and 5, respectively. The initial 25 minutes of each stage, corresponding to the ball seating phase, were not simulated; however, they explain the higher measured initial pressures compared to the hydrostatic pressure in our model. The simulated pumping rates approximate field values but exclude noise and temporary fluctuations.

In the short term, simulated pressures deviate from corrected field data. This discrepancy is attributed to near-wellbore tortuosity, which was not taken into account in the simulations. Fu et al. (2024) demonstrated that short-term pressure predictions could be improved by incorporating the effects of near-wellbore geometry, stress concentrations, fracture initiation, and perforation dynamics.

The long-term predictions from the model exhibited varying degrees of agreement with the field data across the analyzed stages. For Stage 4, the simulated pressures in all scenarios showed general alignment with the field observations after the pumping rate stabilized and fracture propagated beyond the region of stress perturbation by the well and perforations. Not all scenarios successfully captured the pressure drop at approximately 75 minutes. The impermeable cohesive DFN scenario with a reduced initial aperture provided the best prediction of this drop, highlighting the importance of aperture assumptions in modeling fracture behavior.

Stage 5 presented more significant discrepancies. The two scenarios with permeable DFNs significantly underestimated the field pressure. This inconsistency is explained by the intersection of the fracture propagated from Stage 5 with a natural fracture, which subsequently controls the fluid flow and pressure response. Among the evaluated scenarios, the impermeable cohesive DFN with reduced aperture was again the most representative of in-situ conditions, better reproducing the short-term behavior, including the observed breakdown pressure magnitude.

Figures 6 and 7 display microcracking and aperture distributions after 70 minutes of injection in the impermeable cohesive DFN scenario. In Stage 4, a hydraulic fracture formed around the cluster, terminating at two natural fractures above and below. Stage 5 experienced approximately 83% fewer microcracks due to the intersection with a natural fracture, highlighting its influence on hydraulic fracture propagation.

As injection continued after the breakdown pressure was reached and pressure dropped in Stages 4 and 5, pressure increased again as the hydraulic fractures intersected natural fractures, leading to an increase in the aperture of the natural fractures in the intersection area. This behavior is primarily attributed to DFN's strong, initially impermeable, and cohesive characteristics, which resist fluid leakage and

pressure drop. Additionally, the hydraulic fracture created in Stage 3, which exhibits permeable and frictional behavior, was fully reactivated by the end of injection in Stage 5, as shown in Figure 7.

When the initial fracture aperture was reduced by a factor of 10, Stage 4 exhibited increased microcracking, and stimulation in Stage 5 led to the propagation of the existing hydraulic fracture from Stage 4 (Figure 8). However, the hydraulic fracture primarily grew parallel to the natural fractures located above and below it, finding it hard to penetrate them. Additionally, reducing the aperture resulted in reduced pressure increases after the pressure drop compared to the base case, as shown in Figures 4 and 5.

Overall, with or without changes in the aperture, no new hydraulic fractures reached the production well, as seen in Figure 8 (new cutaway view perpendicular to the wells was added). However, reactivation of the hydraulic fracture created in Stage 3 was predicted in both scenarios, confirming fiber optic predictions of connectivity. The fiber optic data suggested fracture hits straight above Stages 4 and 5 and close to Stage 3. Those above Stages 4 and 5 were not predicted in the model, which can be attributed to the stochastic nature of the DFN.

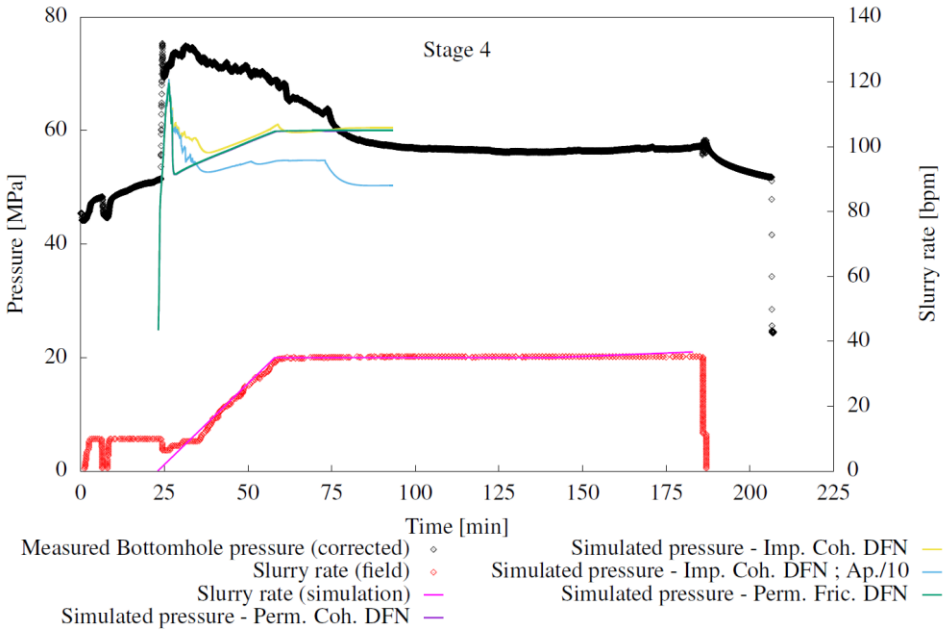

Figure 4 : Measured and Simulated pumping rate and bottomhole pressure histories in Stage 4.

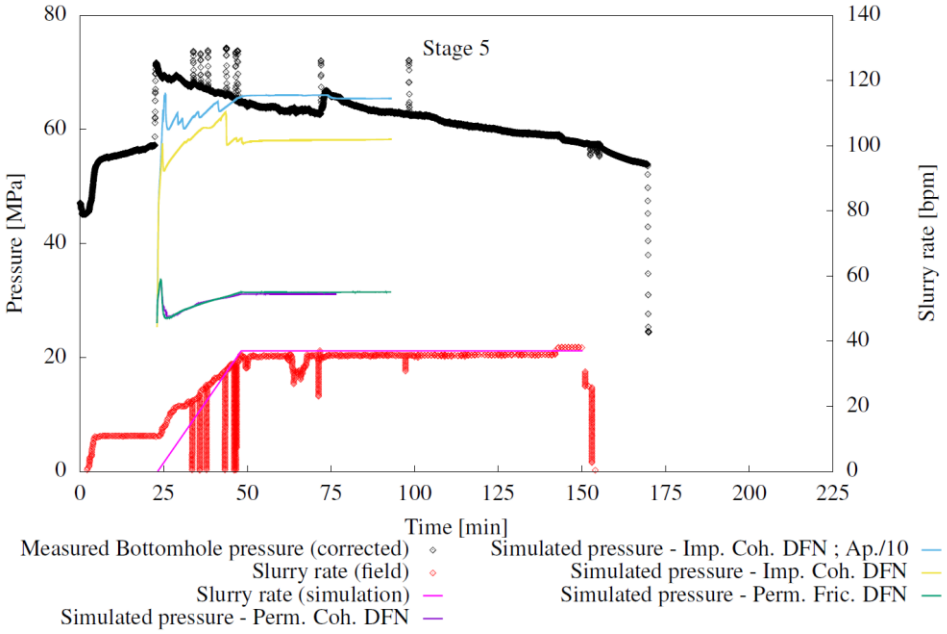

Figure 5 : Measured and Simulated pumping rate and bottomhole pressure histories in Stage 5.

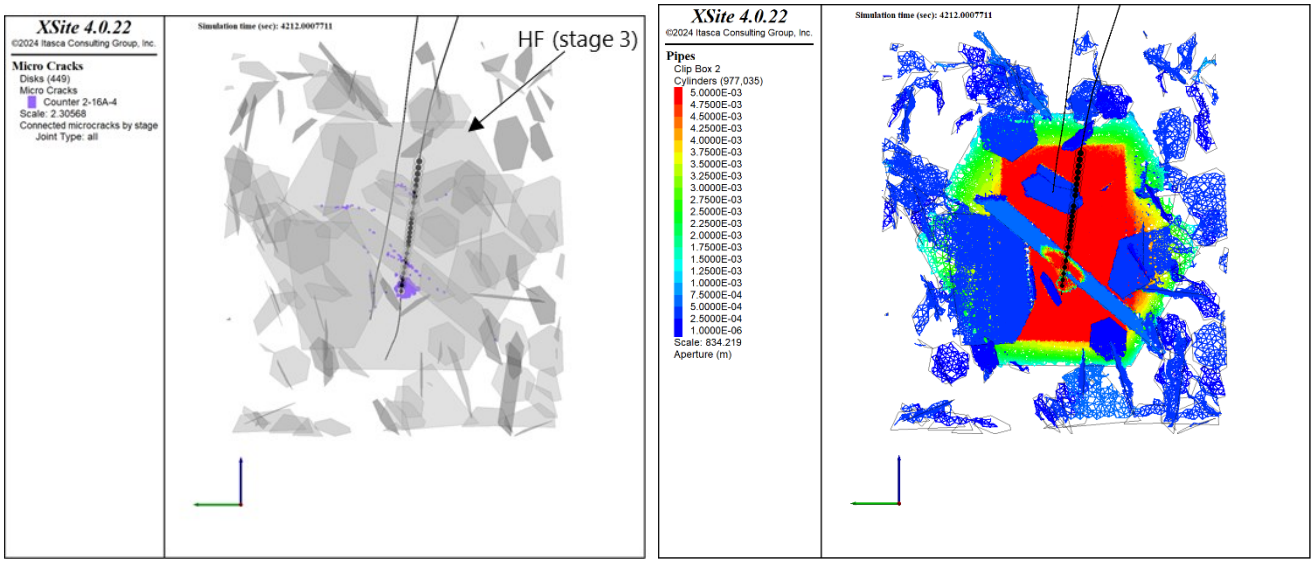

Figure 6 : Cutaway view centered around Stages 4-5 showing microcracking (left) and aperture distribution (right) after 70 minutes of injection in Stage 4 in the case of an impermeable cohesive DFN.

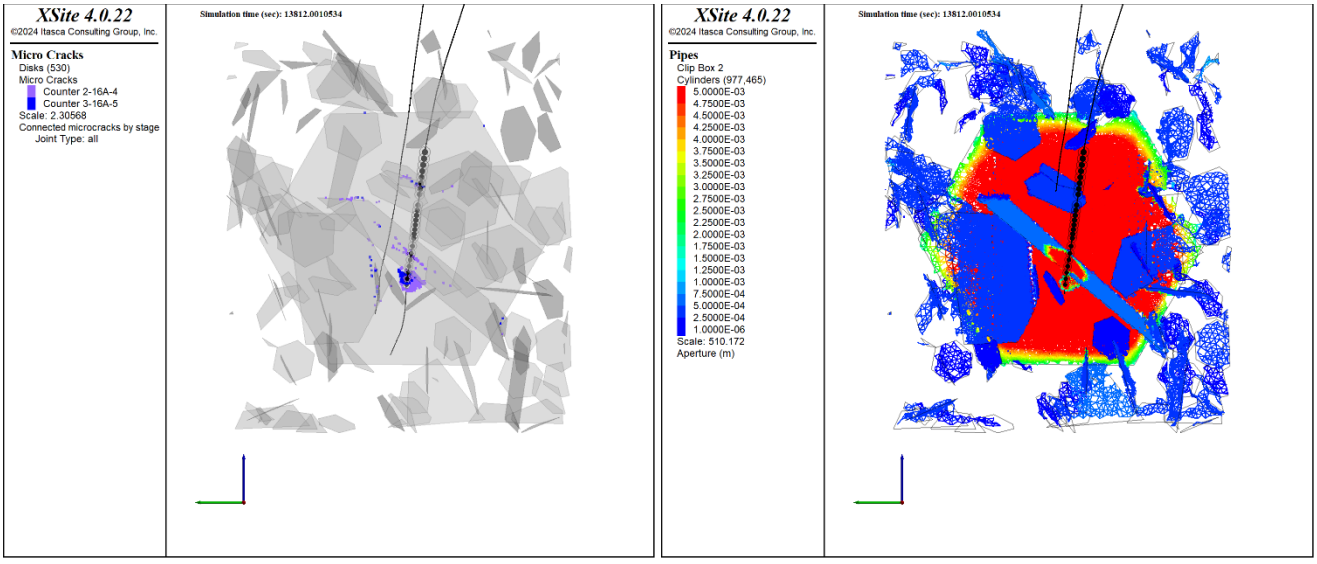

Figure 7 : Cutaway view centered around Stages 4-5 showing microcracking (left) and aperture distribution (right) after 70 minutes of injection in Stage 5 in the case of an impermeable cohesive DFN.

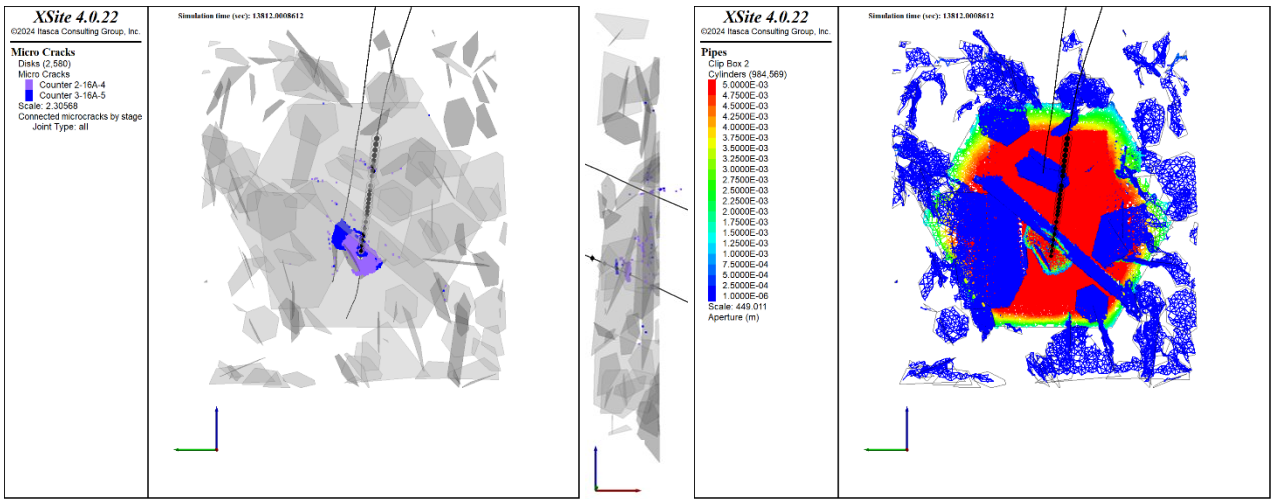

Figure 8 : Two different cutaway views centered around Stages 4-5 showing microcracking (left) and aperture distribution (right) after 70 minutes of injection in Stage 5 in the case of an impermeable cohesive DFN with the initial fracture aperture reduced by a factor of 10.

2.2.2 Stages 8, 9 and 10

The bottomhole injection pressure and pumping rate histories for Stages 8, 9, and 10 are shown in Figures 9, 10, and 11, respectively. These stages were modeled together to account for stress shadow effects from the closely spaced clusters in Stages 8 and 9 and the interactions between hydraulic fractures and the DFN. In Stages 8 and 9, some simulation results showed good agreement with the field data during later pumping times. None of the DFN scenarios fully captured the early injection pressure trend in these stages, likely due to near-wellbore effects and temperature influences, which were not explicitly modeled. However, in Stage 8, the impermeable DFN scenario with reduced initial aperture qualitatively reproduced the same early field bottomhole pressure trend but with a different magnitude.

In Stage 8, the impermeable cohesive DFN with reduced aperture best matched field data in the steady pumping phase, while the permeable DFN scenarios significantly underestimated pressure. In Stage 9, pressure curves from the different scenarios nearly overlapped during the early injection period. In the long term, the two scenarios with permeable DFNs provided the closest match to field data, while the impermeable DFN scenarios overestimated pressure. In Stage 10, the model with an impermeable cohesive DFN with reduced aperture showed good agreement with field data throughout the injection period.

The corrected bottomhole pressure data for Stage 9 are inconsistent with the pressure trends observed in Stages 4,5, 8 and 10, where pressure remained around 60 MPa, while in Stage 9, it was around 50 MPa. This discrepancy may indicate potential measurement errors or a singular reservoir behavior in Stage 9.

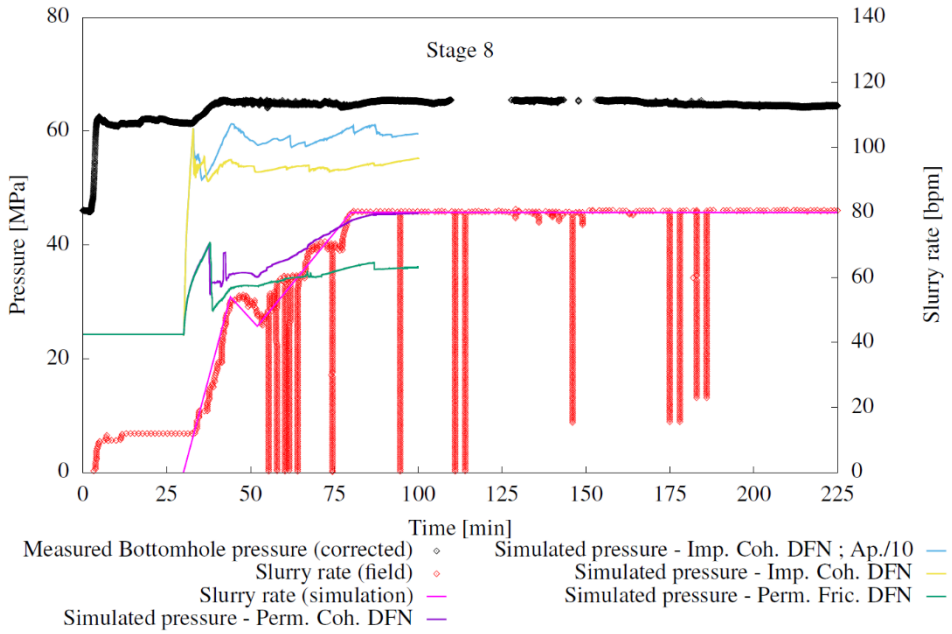

Figure 9 : Measured and simulated pumping rate and bottomhole pressure histories in Stage 8.

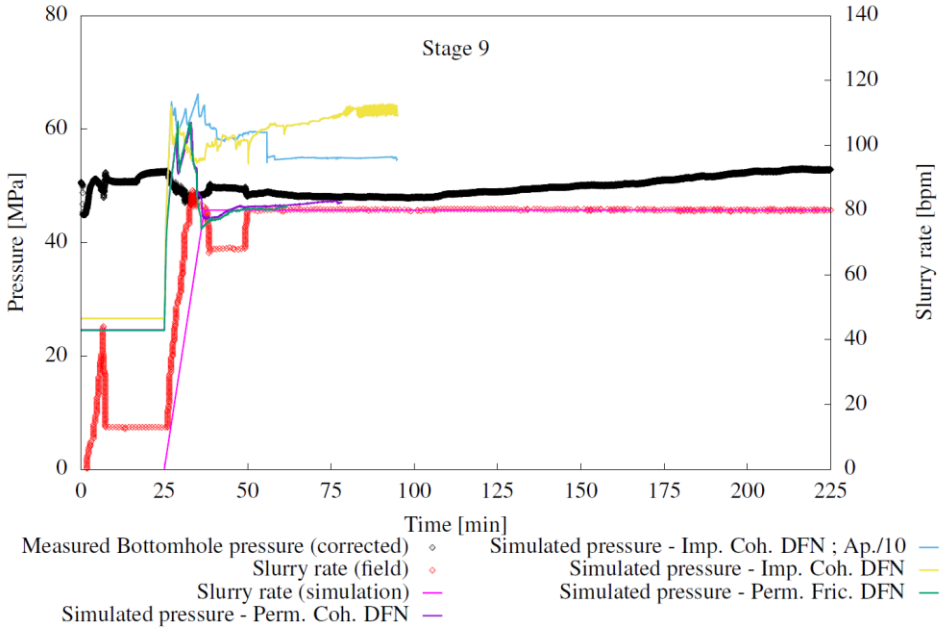

Figure 10 : Measured and simulated pumping rate and bottomhole pressure histories in Stage 9.

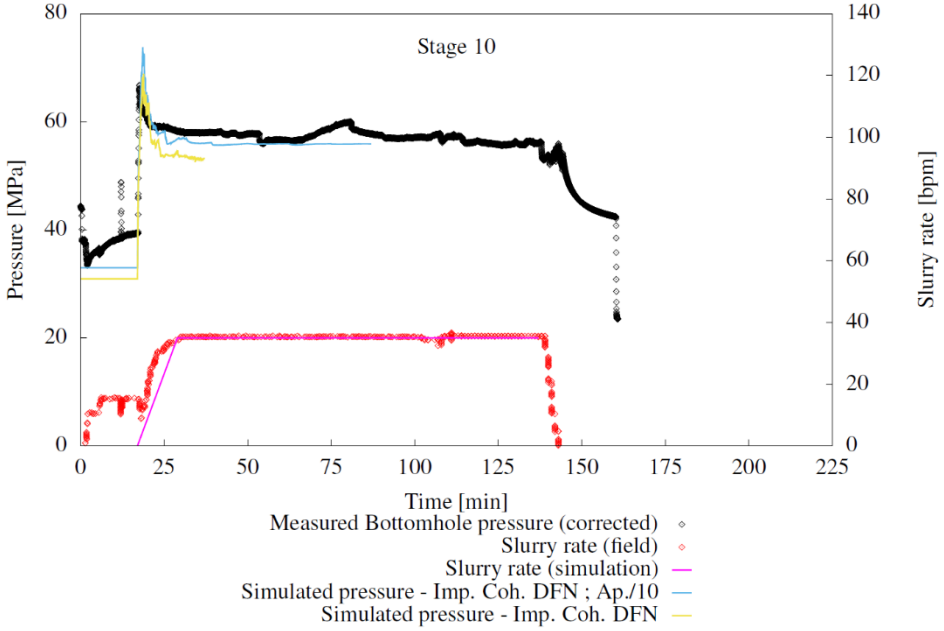

Figure 11 : Measured and simulated pumping rate and bottomhole pressure histories in Stage 10.

Figure 12 presents cropped views from different angles, showing the connected microcracks and aperture distribution after 70 minutes of injection in Stage 8 for two DFN scenarios: the impermeable cohesive DFN with reduced aperture and the permeable cohesive DFN. In the first scenario, most of the microcracking originated from the first five clusters, starting from the toe of the stage. In contrast, minimal microcracking was observed in the last three clusters, raising questions about the effectiveness of closely spaced multi-cluster stages. Microcracking primarily formed hydraulic fractures around the clusters, which were terminated upon intersecting natural fractures. Additionally, microcracking occurred along the borders of natural fractures, facilitating their propagation. Initially impermeable natural fractures were reactivated at their borders and intersection areas with the hydraulic fractures, creating flow paths that were not strictly vertical but instead followed the reactivated natural fracture pathways.

Two primary flow paths developed between Stage 8 and the production well in the model. The first originated from the hydraulic fracture at Cluster 1, which propagated until it was terminated by a nearly vertical natural fracture intersecting the injection well at Cluster 2.

Injection in Stage 8 also reactivated this natural fracture, extending it further. The hydraulic fracture from Cluster 1 and the reactivated natural fracture from Cluster 2 connected and continued propagating upward along a network of intersecting vertical natural fractures. This pathway ultimately extended beyond the production well.

The second main flow path was initiated by Clusters 3, 4, and 5. Since Clusters 3 and 4 did not intersect any natural fractures, they propagated hydraulic fractures, which deviated slightly westward due to stress shadowing and nearby natural fractures. These fractures then connected with pre-existing fractures reactivated by Cluster 5, including both vertical and horizontal ones, forming a complex fracture network that integrated hydraulic and natural fractures. As this network evolved, the reactivated fractures propagated further, shifting the intersection with the production well westward, aligning with the first cluster of Stage 9. This westward shift of the intersection, rather than being directly aligned with the injection clusters, demonstrates how natural fractures influence connectivity between stages, significantly altering fluid pathways and extending the reach of hydraulic fractures.

Fiber optic measurements (Figure 2) detected multiple hit events. Two of these hits were aligned with Stage 8 clusters, while additional hits were recorded above the last clusters of Stage 9 and above Stage 10. The impermeable cohesive DFN with reduced aperture scenario correctly predicted the location of the first hit aligned with Stage 8 clusters. However, in the model, the second intersection occurs between the locations of the second and third hits recorded by fiber optic—where the second hit is above the last cluster of Stage 8 and the third is above the mid-length of Stage 9. While this scenario captured part of the observed fracture connectivity, it did not exactly reproduce the additional hits recorded above Stages 9 and 10, which was not expected considering a stochastic nature of the DFN.

For comparison, Figure 12 presents result from the permeable cohesive DFN scenario, which predicts widespread fault reactivation above Stage 8 and only sparse microcracking with no hydraulic fracturing —an outcome that appears somewhat unrealistic. While this scenario correctly predicts only the first fiber optic hit, it also reactivates multiple natural fractures with different orientations above Stage 9. None of these fractures appear to vertically intersect the production well, but some reactivated vertical and parallel fractures are positioned 30 m away from it.

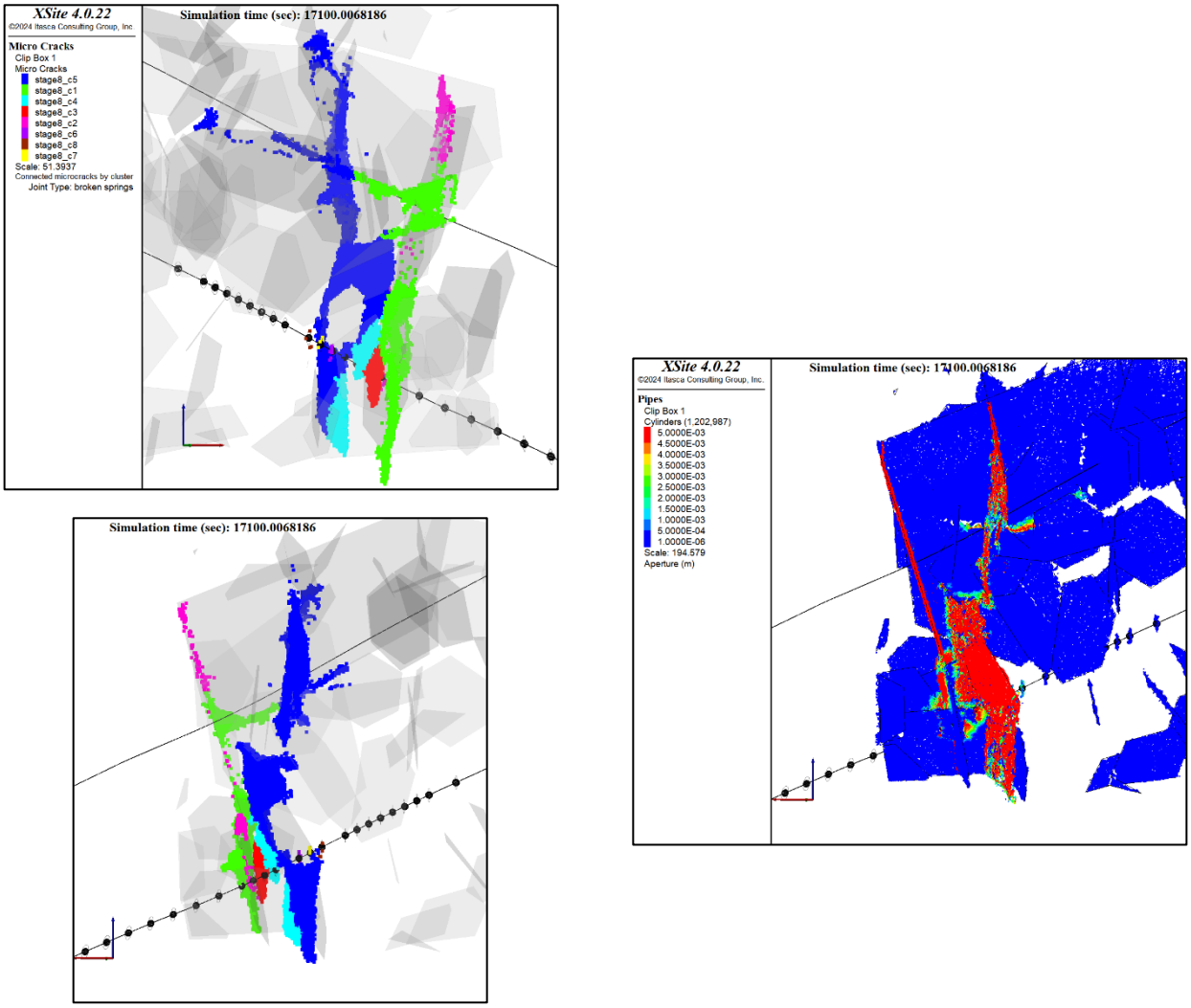

Impermeable Cohesive DFN, reduced initial aperture

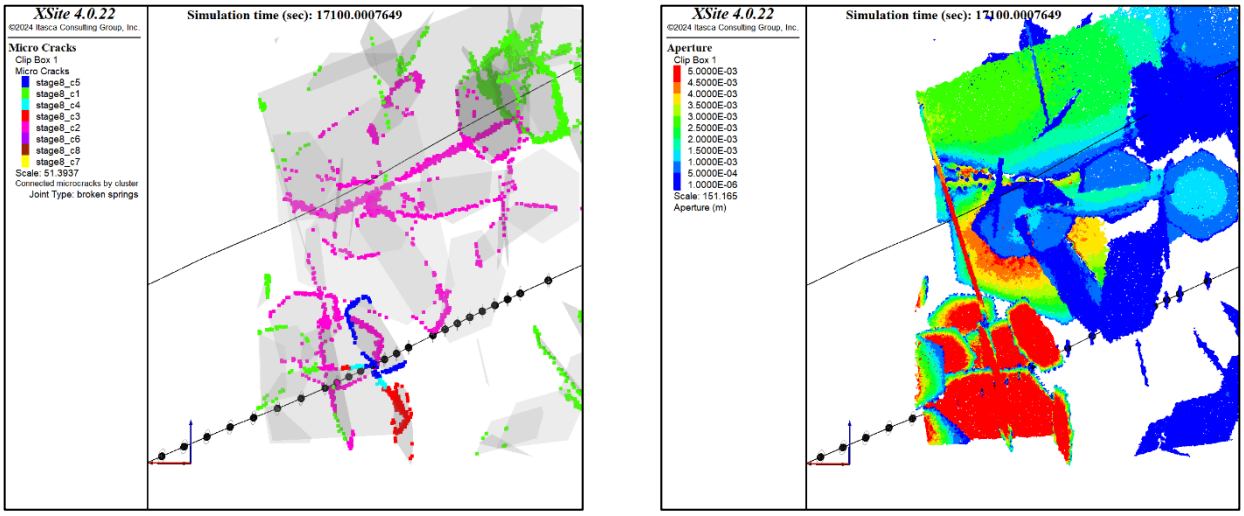

Permeable Cohesive DFN

Figure 12 : Cutaway view centered around Stages 8, 9, and 10, showing microcracking (left) and aperture distribution (right) after 70 minutes of injection in Stage 8 for two DFN scenarios. All views are from an angle looking south, except the first one, which is from an angle looking north.

Figure 13 presents the microcracks and aperture distribution after 70 minutes of injection in Stage 9 for the impermeable cohesive DFN scenario with reduced initial aperture. An additional flow path is predicted, following reactivated natural fracture paths that bend westward and extend further up—not directly above Stage 10, but beyond it. This path originates from the seventh and eighth clusters, where hydraulic fractures interact with natural fractures, facilitating their reactivation and upward propagation to intersect the production well. At the production well, the intersection shows multiple branches due to the influence of existing natural fractures, which may account for the multiple closely spaced hits observed in the fiber optic data (Figure 2).

In Stage 10, a hydraulic fracture forms around the cluster and connects with the hydraulic fracture network from Stage 9, creating a single, extensive flow network. As a result, stimulation in Stage 10 increased the overall extent of the connected fracture network, as evidenced by the areas with larger apertures shown in Figure 14.

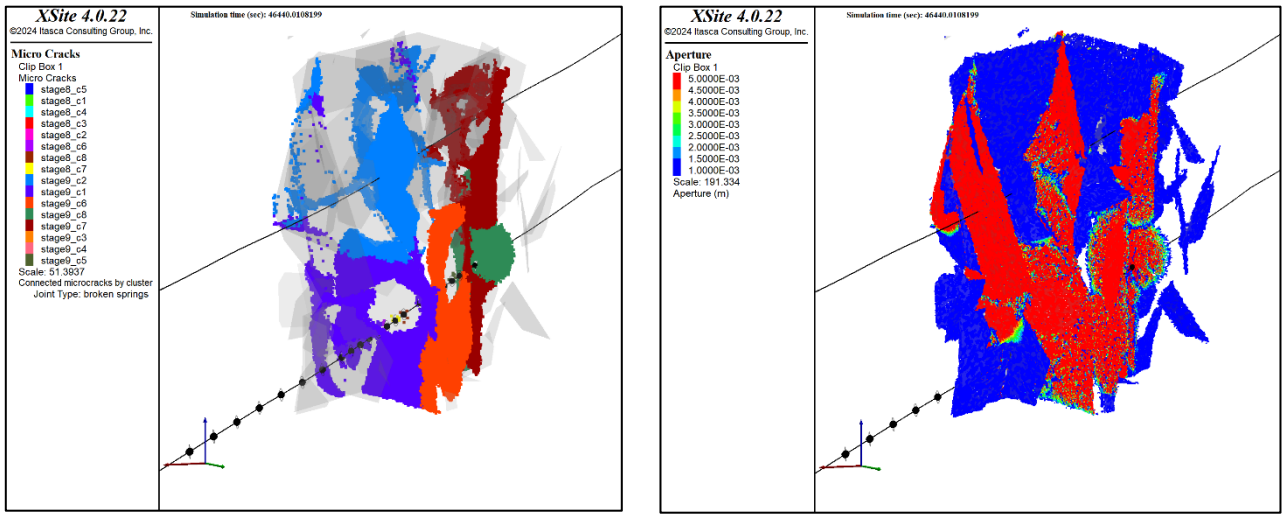

Figure 13 : Cutaway view centered around Stages 8-9-10 (looking south) showing microcracking (left) and aperture distribution (right) after 70 minutes of injection in Stage 9 in the impermeable cohesive DFN scenario with reduced initial aperture.

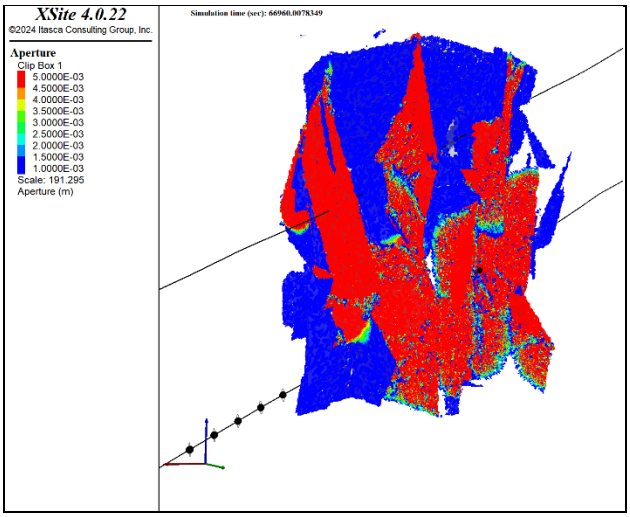

Figure 14 : Cutaway view centered around Stages 8-9-10 (looking south) showing aperture distribution after 70 minutes of injection in Stage 10 in the impermeable cohesive DFN scenario with reduced initial aperture.

3. CONCLUSION

This study investigated the influence of DFN characteristics on hydraulic stimulation at the Utah FORGE site using coupled hydro-mechanical modeling in XSite. The results indicate that the frictional or cohesive nature of fractures has a limited impact on the reservoir stimulation and injection pressure response. Instead, the initial permeability of natural fractures plays a critical role in controlling the pressure history and fluid migration.

Among the DFN scenarios considered, the impermeable cohesive DFN with reduced initial aperture best approximates the observed long-term bottomhole pressures. While some discrepancies remain, particularly in Stage 9, these may stem from uncertainties in pressure corrections rather than inaccuracies in the model itself. This scenario also resulted in more localized fracture activation and the formation of four primary flow pathways between the injection and production wells: one in Stages 4-5 and three in Stages 8-9-10. While these pathways align with fiber optic hits observed in fiber optic data, the model does not fully capture all observed connectivity. In contrast, permeable DFN scenarios led to excessive fracture reactivation, producing unrealistic fluid dispersion.

To further assess the validity of the impermeable cohesive DFN, future work should incorporate shut-in periods to evaluate fracture closure effects. Additionally, microseismic data should be used to compare numerical modeling results, while both microseismic and fiber optic data should guide updates to the DFN to improve its representation of the natural fracture network. These refinements will strengthen confidence in the model's predictive capabilities and provide a more accurate assessment of stimulation-driven flow pathways at FORGE.

ACKNOWLEDGEMENTS

Funding for this work was provided by the U.S. Department of Energy under grant DE-EE0007080 "Enhanced Geothermal System Concept Testing and Development at the Milford City, Utah FORGE Site." We thank the many stakeholders supporting this project, including Smithfield, Utah School and Institutional Trust Lands Administration, and Beaver County, as well as the Utah Governor's Office of Energy Development.

This research made use of the resources of the High Performance Computing Center at Idaho National Laboratory, which is supported by the Office of Nuclear Energy of the U.S. Department of Energy and the Nuclear Science User Facilities under Contract No. DE-AC07-05ID14517.

REFERENCES

Damjanac, B., & Cundall, P.: Application of Distinct Element Methods to Simulation of Hydraulic Fracturing in Naturally Fractured Reservoirs, Computers and Geotechnics, 71, (2016), 283–294. https://doi.org/10.1016/j.compgeo.2015.06.007

Finnila, A., Doe1, T., Podgorney, R., Damjanac, B. and Xing, P.: Revisions to the Discrete Fracture Network Model at Utah FORGE Site, Proceedings, Geothermal Rising Conference: Using the Earth to Save the Earth, GRC 2021, San Diego, CA (2021).

Finnila, A., and Jones, C.: Updated Reference Discrete Fracture Network Model at Utah FORGE, Proceedings, 49th Workshop on Geothermal Reservoir Engineering, Stanford University, Stanford, CA (2024).

Fu, W., Damjanac, B., Radakovic-Guzina, Z., Finnila, A., Podgorney, R. and Mclennan, J.: Near-Wellbore DEM Model of Hydraulic Fracture Initiation for Utah FORGE Site, Proceedings, 49th Workshop on Geothermal Reservoir Engineering Stanford University, Stanford, CA (2024).

Fu, W., Savitski, A. A., Damjanac, B., & Bunger, A. P.: Three-Dimensional Lattice Simulation of Hydraulic Fracture Interaction with Natural Fractures, Computers and Geotechnics, 107, (2019). 214–234. https://doi.org/10.1016/j.compgeo.2018.11.023

Fu, W., Ames, B. C., Bunger, A. P., & Savitski, A. A.: Impact of Partially Cemented and Non-persistent Natural Fractures on Hydraulic Fracture Propagation, Rock Mechanics and Rock Engineering, 49(11), (2016), 4519–4526. https://doi.org/10.1007/s00603-016-1103-0

Itasca: XSite-Hydraulic Fracture Simulation of 3D Fracture Networks (4.0), Minneapolis, Minnesota (2023).

McLennan, J., Swearingen, L., and England, K.: Utah FORGE: Wells 16A(78)-32 and 16B(78)-32 Stimulation Program Report - May 2024, (2024). https://doi.org/10.15121/2483880

Niemz, P., Pankow, K., Isken, M., Whidden, W., McLennan, J. and Moore, J.: Mapping Fracture Zones with Nodal Geophone Patches: Insights from Induced Microseismicity During the 2024 Stimulations at Utah FORGE, Seismological Research Letters, (2025). https://doi.org/10.1785/0220240300

Xing, P., Damjanac, B., Radakovic-Guzina, Z., Torres, M., Finnila, A., Podgorney, R., Moore, J. and McLennan, J.: Comparison of Modeling Results with Data Recorded During Field Stimulations at Utah FORGE Site, Proceedings, 48th Workshop on Geothermal Reservoir Engineering, Stanford, CA (2023).